Permeability evolution during progressive development of deformation bands in porous sandstones

Permeability evolution during progressive development of deformation bands in porous sandstones

B. T. Ngwenya
School of GeoSciences, Institute of Geology and Geophysics, University of Edinburgh, Edinburgh, UK

O. Kwon
Core Laboratories, Houston, Texas, USA

S. C. Elphick and I. G. Main
School of GeoSciences, Institute of Geology and Geophysics, University of Edinburgh, Edinburgh, UK

Received 4 March 2002; revised 5 August 2002; accepted 12 February 2003; published 22 July 2003.

[1] Triaxial deformation experiments were carried out on large (0.1 m) diameter cores of a porous sandstone in order to investigate the evolution of bulk sample permeability as a function of axial strain and effective confining pressure. The log permeability of each sample evolved via three stages: (1) a linear decrease prior to sample failure associated with poroelastic compaction, (2) a transient increase associated with dynamic stress drop, and (3) a systematic quasi-static decrease associated with progressive formation of new deformation bands with increasing inelastic axial strain. A quantitative model for permeability evolution with increasing inelastic axial strain is used to analyze the permeability data in the postfailure stage. The model explicitly accounts for the observed fault zone geometry, allowing the permeability of individual deformation bands to be estimated from measured bulk parameters. In a test of the model for Clashach sandstone, the parameters vary systematically with confining pressure and define a simple constitutive rule for bulk permeability of the sample as a function of inelastic axial strain and effective confining pressure. The parameters may thus be useful in predicting fault permeability and sealing potential as a function of burial depth and fault displacement. *INDEX TERMS:* 5112 Physical Properties of Rocks: Microstructure; 5114 Physical Properties of Rocks: Permeability and porosity; 5139 Physical Properties of Rocks: Transport properties; 8010 Structural Geology: Fractures and faults; 8020 Structural Geology: Mechanics; *KEYWORDS:* permeability, deformation bands, fractures, shear bands, fault seal

Citation: Ngwenya, B. T., O. Kwon, S. C. Elphick, and I. G. Main, Permeability evolution during progressive development of deformation bands in porous sandstones, *J. Geophys. Res.*, *108*(B7), 2343, doi:10.1029/2002JB001854, 2003.

1. Introduction

[2] Faults provide major control on the timing and movement of fluids in the subsurface [*Knipe*, 1992]. As a result, knowledge of the permeability of faults and how this evolves in time and space is critical in solving practical problems and understanding natural geological processes [*Tuefel*, 1987]. Geologic evidence suggests that the hydraulic properties of faults evolve continuously in space and time, so that a single fault may have been both a conduit and a seal at different times in its history [*Evans et al.*, 1997; *Ngwenya et al.*, 2000]. Temporal variability is implicit in classical mechanisms that have been suggested for episodic fluid flow and mineralization, including crack-seal veining [*Ramsay*, 1980], seismic valving [*Sibson*, 1992], and primary hydrocarbon migration [*Hippler*, 1993]. On the other hand, *Caine et al.* [1996] have linked spatial variability in fault permeability to fault zone architecture, which is itself a function of several variables, including rock type/composition, state of stress, shear strain, and/or microstructural deformation mechanisms.

[3] Our knowledge of the evolution of fault zones in porous sandstones has advanced significantly over the last 20 years or so. Field studies have identified a consistent sequence in which fault zones evolve from single deformation bands through zones of deformation bands to slip surfaces with increasing shear offset [*Aydin*, 1978; *Aydin and Johnson*, 1978; *Underhill and Woodcock*, 1987; *Antonellini and Aydin*, 1994; *Shipton and Cowie*, 2001]. This sequence has been attributed to an interplay between local strain hardening and strain softening mechanisms, where reduction in grain size and the attendant increase in contact area within a deformation band leads to strengthening of the band, so that further failure occurs outside the existing band [*Aydin and Johnson*, 1978; *Mair et al.*, 2000]. Thus deformation bands, which are thin and laterally continuous structures with localized cataclasis and/or compaction not

0148-0227/03/2002JB001854$09.00

only initiate the faulting process but are also abundant around major faults formed at shallow crustal depths (brittle field) in porous sandstones [*Knott et al.*, 1996; *Beach et al.*, 1999].

[4] The presence of deformation bands introduces a high degree of complexity to the permeability structure of a fault zone even at a single point in time [*Caine et al.*, 1996]. In particular, measurements of permeability of fault zones at both outcrop [e.g., *Antonellini and Aydin*, 1994] and core scale [e.g., *Fowles and Burley*, 1994; *Gibson*, 1998] show significant permeability anisotropy that can lead to fluid compartmentalization in otherwise permeable host rocks [*Knipe et al.*, 1998]. Moreover, the degree of permeability anisotropy observed may depend on the methods used, with high spatial resolution techniques yielding higher permeability contrasts between host rocks and fault zones [*Ogilvie et al.*, 2001].

[5] Unfortunately, outcrop and core-scale measurements only indicate a final snapshot of the permeability structure, and give no insight into the time-dependent history of the fault. As pointed out above, the latter depends strongly not only on host rock composition but also on complex interaction among a suite of external variables, including stress, temperature, strain and fluid composition [*Main et al.*, 1994]. Because these interactions are not separable from an outcrop measurement, the key to understanding the temporal evolution of permeability is to conduct controlled laboratory tests in which permeability is measured during progressive development of the fault. Previous studies of this type [e.g., *Zhu and Wong*, 1997] have not captured all of the critical steps in the evolution of natural fault zones in porous sedimentary rocks. Specifically, the complex three-dimensional (3-D) structure of natural deformation bands has only been reported in experiments conducted at pressures near the brittle-ductile transition zone [*Scott and Nielsen*, 1991; *Jamison and Stearns*, 1992; *Wong et al.*, 1997]. Away from this narrow transition zone the deformation takes the form of either localized cataclasis (a single deformation band) or distributed shear compaction in the brittle and ductile regimes respectively [*Wong et al.*, 1997].

[6] However, recent experiments suggest that this discrepancy between natural and experimental fault zone structures may be an artefact of sample size [*Mair et al.*, 2000; *Main et al.*, 2000]. By deforming large, 10 cm diameter samples to varying ultimate axial strains, natural fault zone structures could be reproduced, both in terms of geometrical complexity normal to the fault plane, and in the increase in the number (n) of deformation bands (strands) with increasing strain. The latter was consistent with a linear relation of the form

$$n = n_o(\varepsilon - \varepsilon_c), \tag{1}$$

where ε is the axial strain (defined positive for shortening), ε_c is the axial strain at dynamic failure, and n_o is the rate of formation of deformation bands per unit axial strain. It has been suggested that the larger sample size may allow for a greater number of solutions for the strain accommodation problem and allow lower strain rates closer to those applicable to natural deformation [*Main et al.*, 2001]. Grain-size analysis of the individual deformation bands revealed that all deformation bands for a given rock type at a constant confining pressure had the same grain-size distribution, regardless of total axial strain [*Mair et al.*, 2000]. This is consistent with a steady state grinding process, which results in a relatively constant porosity and permeability for individual deformation bands, although this model may not always necessarily hold in the field.

[7] *Main et al.* [2000] used these microstructural observations to develop a simple geometrical model for permeability changes with increasing inelastic axial strain, allowing the evolution of permeability to be experimentally quantified as a function of increasing fault zone complexity. The basic assumptions of the model, which were verified by the data, were that (1) for any strain ($\varepsilon - \varepsilon_c$) above the critical strain ε_c, the total effective width of the fault zone is $w = nw_{strand}$, where w_{strand} is the width of an individual band; (2) the number of bands increases linearly with postfailure strain, so that $w = w_0(\varepsilon - \varepsilon_c)$, where w_0 is the rate at which the fault zone width increases per unit strain; (3) the bulk sample may either dilate at low confining pressure or compact at high confining pressure and, consequently, the permeability of the matrix (k_{matrix}) can increase or decrease during dilation or compaction, respectively; (4) the porosity of each strand is constant so that k_{strand} stays constant with increasing inelastic axial strain; and (5) permeability varies exponentially with porosity over the small range of porosity changes measured.

[8] The results of *Main et al.* [2000] showed that the volumetric strain (Δ) and hence porosity varied linearly with postfailure strain. Since the porosity of the deformation bands does not change systematically with postfailure strain [*Mair et al.*, 2000], the strain-dependent matrix permeability takes the form

$$k_{matrix} = k_c \exp[-\gamma_I(\varepsilon - \varepsilon_c)], \tag{2}$$

where k_c is the permeability (m^2) at critical strain and γ_I is the inelastic strain sensitivity parameter for the matrix in the postfailure stage. The bulk permeability (k_{bulk}) of the whole sample could then be estimated by using a geometric mean of the permeability of the individual components (matrix and deformation bands) of the total path length [e.g., *Gibson*, 1998; *Manzocchi et al.*, 1999], leading to (see *Main et al.* [2000] for full derivation)

$$\ln k_{bulk} = \ln k_c + a_1\left(\frac{\delta}{1-\delta}\right) + a_2\left(\frac{\delta^2}{1-\delta}\right), \tag{3a}$$

where

$$a_1 = -\left[\frac{w_0(\ln k_c - \ln k_{strand})}{l_c} + \gamma_I\right] \tag{3b}$$

and

$$a_2 = \gamma_I\left(1 + \frac{w_0}{l_c}\right). \tag{3c}$$

In equation (3), l_c is the sample length at critical strain (ε_c), δ is the inelastic axial strain equal to $\varepsilon - \varepsilon_c$, while a_1 and a_2 are constants and permeabilities are all in m^2. Equation (3) constitutes a model for the evolution of permeability with

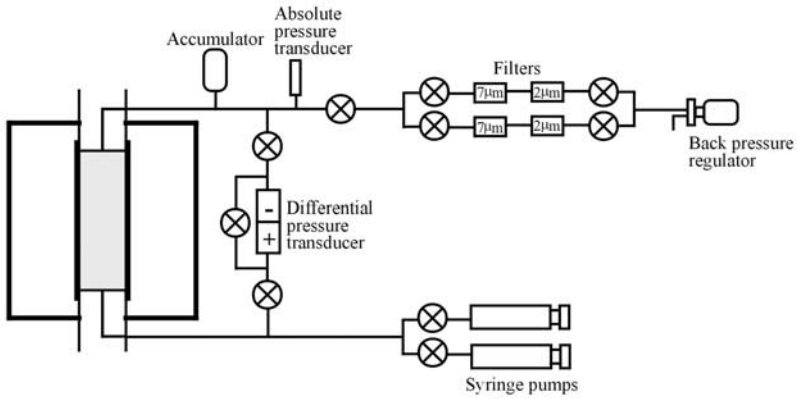

Figure 1. Schematic layout of the large capacity deformation rig, with permeameter for steady state permeability measurements.

postfailure axial strain at a constant confining pressure, and contains two free parameters a_1 and a_2, from which the physical quantities γ_I and k_{strand} may be evaluated, provided that w_0 and l_c can be obtained from the data.

[9] While equation (3) has been shown to statistically provide a good description of experimental data in a previous communication [*Main et al.*, 2000], it has not been fully tested under a range of confining pressures. This is important because deformation style varies systematically with depth [*Antonellini et al.*, 1994], as confirmed by recent laboratory tests [*Mair et al.*, 2002]. In this paper, we report data on a systematic study in which permeability was measured as a function of axial strain at different effective confining pressures. The objectives were (1) to characterize the evolution of permeability during deformation to varying strains and validate our recent model, (2) to relate the changes observed to the geometry of the fault zone, and (3) to show how the effective confining pressure affects permeability evolution and hence model parameters. The results show that a_1 and a_2 do vary systematically with effective confining pressure and thus provide a simple constitutive rule for predicting permeability as a function of burial depth and inelastic axial strain in high-porosity sandstones.

2. Experimental Methods

2.1. Test Samples

[10] The experiments were carried out on cores of the Clashach sandstone from northeast Scotland. This sandstone is essentially an arkosic arenite, of Permian age and aeolian in origin, consisting of about 90% quartz and 10% K-feldspar [*Ngwenya et al.*, 1995] ranging from 250 to 500 μm in grain diameter. Both minerals are largely of detrital origin, although significant quartz cementation in the form of overgrowths is present, producing a sandstone with porosities of 12–18% and permeabilities ranging from 2×10^{-13} to just over 10^{-12} m^2 [*Ngwenya et al.*, 2000]. The sandstone therefore differs slightly from the one used by *Mair et al.* [2000], mainly in terms of diagenetic mineral assemblage and/or lower porosity [*Ngwenya et al.*, 2000].

[11] Core samples were prepared from a single block to a length to diameter ratio of at least 2.25/1 and were end faced in a lathe but were not polished. Initial connected porosity was determined by taking the difference in weight of a sample after and before saturation with distilled water, assuming a value of 1000 kg/m^3 for the density of distilled water.

2.2. Experimental Procedure

[12] Details of the experimental apparatus and deformation procedure were essentially the same as those given by *Mair et al.* [2000], with modifications to allow for permeability measurements. The total load on the sample was measured using two load cells rated to 2MN. Confining pressures up to 70 MPa could be applied to the cylindrical face of the sample, while the self-balanced ram ensured that the sample was also end loaded to hydrostatic confinement prior to deformation. Deformation was conducted using displacement control, with a constant axial strain rate of $\sim 5 \times 10^{-6}$ s^{-1}. An internal linear variable differential transformer (LVDT) measures axial displacement of the sample during deformation.

[13] Pore pressure was controlled independently and maintained at 6.9 ± 0.5 MPa using a constant flow rate, single-stroke ISCO™ syringe pump working against a back-pressure regulator downstream of the sample (Figure 1). The flow rates used ranged from 0.5 to 6 cm^3/min, corresponding to Reynolds numbers of 1 to 13. High-sensitivity Validyne DP360 differential pressure transducers (±50, ±125, and ±300 pounds per square inch differential, 1 psi = 0.0069 MPa) were used to measure pore pressure differences across the bulk sample. The measured differential pressures were used to calculate the bulk permeability of the core using the steady state form of Darcy's law [*Rhett and Teufel*, 1992]. Volumetric strain and hence porosity were calculated from volume changes in the confining pressure intensifier that were required to maintain a constant confining pressure on the sample. Although the piston in the confining pressure intensifier is monitored by a very accurate (0.5% error) LVDT, the actual piston movements reflect time-integrated changes in the sample as well as seals (stick-slip) and confining rubber liners. This, combined with the small volume changes measured overall, introduces some scatter in the volumetric strain data. The resulting error was estimated by linear regression of the volumetric strain data

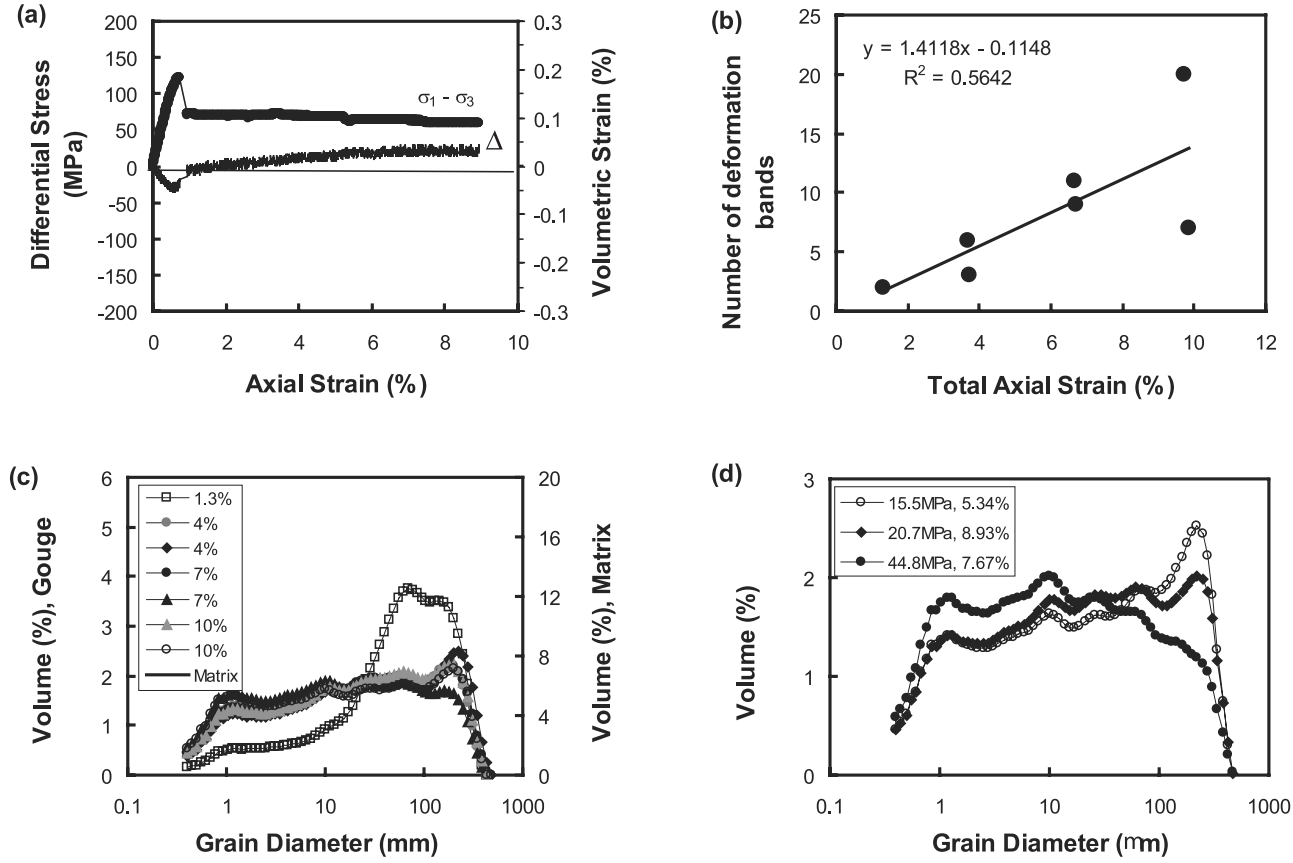

Figure 2. (a) Differential stress ($\sigma_1 - \sigma_3$) and volumetric strain (Δ) plotted against axial strain for sample CLS15. The stress postfailure is essentially quasi-static, while the sample dilates with increasing axial strain. (b) Number of deformation bands as a function of total axial strain. The number of deformation bands increases linearly with total axial strain at a rate of 1.4 bands per unit axial strain. Grain-size distribution of gouge collected from fault zones for (c) samples deformed to varying total axial strains and (d) samples deformed at different effective confining pressures. Notice that a second *y* axis is used for matrix grain-size distribution in Figure 2c. The final grain-size distribution appears to be independent of total final strain once the axial strain exceeds 4% (Figure 2c), but the percentage of fine grains increases and that of large grains dramatically decreases with increasing effective confining pressure (Figure 2d).

in the linear-elastic part of the stress-strain curve against the LVDT for the main piston, and is of the order of 20%.

2.3. Microstructural and Grain-Size Analysis

[14] Deformed samples were carefully removed from the deformation apparatus, dried to constant weight and cut perpendicular to the long axes while still encased in their rubber sleeves. The cut surfaces were photographed before removal of rubber sleeves and deformation band patterns on the cut surfaces, and lateral surfaces were examined. Subsequently, one half of each sample was split along the fault and gouge materials were collected from individual deformation bands for particle size analysis to investigate gouge evolution with increasing axial strain. A Coulter LS100 Laser Particle Size Analyser with a range of 0.4–1000 μm was used for grain-size analysis, and particles of the undeformed samples were also analyzed for comparison.

[15] Thin sections were made from the second half of the core, parallel to the axial loading direction and perpendicular to the fault, after impregnating the samples with epoxy resin. These were examined under the electron microscope in backscattered mode in order to facilitate visualization of the fault geometry in more detail and to examine microstructures associated with deformation.

3. Results

3.1. Mechanical and Microstructural Observations

[16] *Mair et al.* [2000] first described microstructural features of fractures developed under air-dry conditions during triaxial deformation of large diameter samples at varying inelastic axial strains and reported an evolutionary history, which mimicked field observations. It was found that the width of the fracture zone increased linearly with inelastic axial strain for experiments conducted at a constant confining pressure, consistent with previous studies on smaller samples [e.g., *Tuefel*, 1987]. The increase in fracture width was due to progressive increase in the number of discrete strands of comminuted country rock with small offset, rather than due to frictional wear and widening along a single strand [*Scholz*, 1987]. The number of strands was highly correlated with axial strain according to equation (1), with n_o = 1.26. Grain-size analysis showed that the individual strands evolved to a relatively constant grain-size

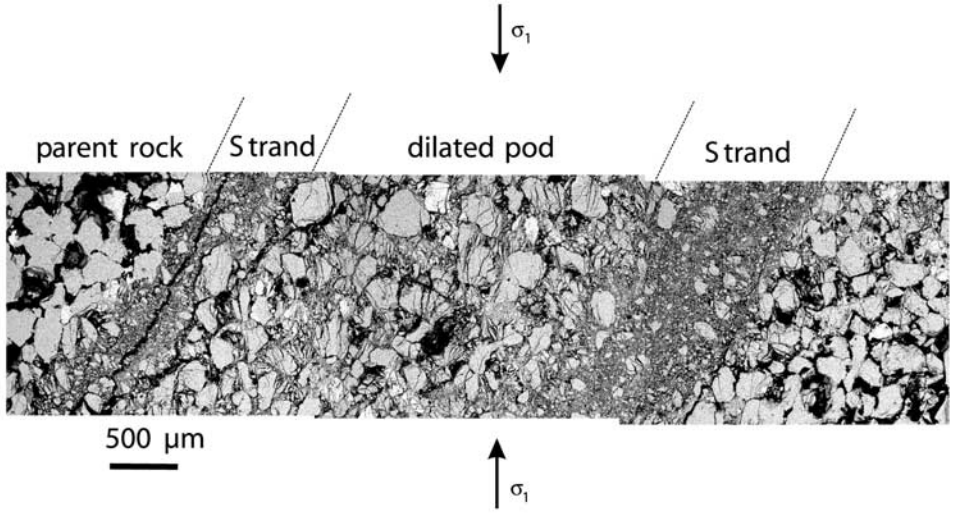

Figure 3. A mosaic of several photographs taken across the fault zone in a thin section of one of the samples deformed to high strain. Note the high density of axial microcracks in the dilated pods between the deformation bands (strands) and also in the parent rock on the right side of the large strand. The strands show grain comminution, while the microfracturing in pods between the strands may be responsible for some of the postfailure dilatancy. The strand on the left also shows open ''fractures'' probably resulting from unloading or introduced during thin sectioning.

distribution of angular, interlocking fragments, implying local strain hardening in each comminuted strand and a relatively constant permeability for each individual strand. However, it was unclear as to whether these features were unique to the relatively weak and high-porosity (22%) Locharbriggs sandstone used in their experiments, or whether such structures would be affected by the presence of a pore fluid.

[17] In fact, our experiments on Clashach sandstone are consistent with the results of *Mair et al.* [2000]. Figure 2a shows the differential stress ($\sigma_1 - \sigma_3$) and volumetric strain (Δ) for a sample deformed to about 5% axial strain. Initially, the sample compacts at a constant rate during the elastic phase of deformation. This phase is followed by dilatant strain hardening to a peak stress at about 0.8% strain, after which we observe a dynamic stress drop, which is associated with a major increase in volumetric strain. Subsequently, the volumetric strain increases at a constant rate, while the differential stress remains essentially constant.

[18] The number of deformation bands (strands) increases with increasing axial strain, in this case, at a rate (n_o) of 1.4 per unit axial strain (Figure 2b). Meanwhile, the particle size distribution remains relatively constant, with log-periodic peaks at 1, 10, and 100 μm (Figure 2c) and two further smaller peaks between 10 and 100 μm. Our results thus conform to the model of *Mair et al.* [2000], where slip is accumulated by an increase in the number of deformation bands (Figure 2b), and no significant boundary strain softening or hardening is seen on the loading platens during the formation of individual bands. The latter implies that strain hardening and/or softening mechanisms are very localized within or near the band itself [*Main et al.*, 2001]. This similarity with the observations of *Mair et al.* [2000] suggests that the presence of a pore fluid and the use of a different rock type do not alter the essential characteristics of the fault zone development and the microstructural properties of the bands.

[19] The effect of increasing effective confining pressure is to systematically increase the proportion of grains finer than ~10 μm (Figure 2d), associated with a transition to more pervasive grain fracturing [*Mair et al.*, 2002]. This is indicative of an increase in ''cataclastic intensity'' that can be directly related to the resolved normal stress on the fault [*Tuefel*, 1987; *Crawford*, 1998]. At effective confining pressures greater than 100 MPa, porous sandstones tend to fail by pervasive grain crushing in shear-enhanced compaction along a critical state curve [*Wong et al.*, 1997]. However, most of our experiments were carried out at confining pressures within the dilatant brittle field, although we see a tendency toward relatively more pervasive deformation at our highest effective confining pressure (45 MPa) in the mechanical data and microstructural properties (see section 4).

[20] Microstructural examinations of thin sections confirm the multiple deformation bands seen in hand specimens (Figure 3), with strands of comminuted rock enclosing lenses of host rock which contain significantly increased density of axial microcracks. Meanwhile, the area bordering the shear fault is sometimes significantly dilated, with microcracks whose density decreases with distance from the fault, consistent with observations in other studies [e.g., *Moore and Lockner*, 1995; *Ngwenya et al.*, 2000; *Zang et al.*, 2000]. This microcrack induced dilation may explain the increase in volumetric strain seen in most of our samples with increasing axial strain (Figure 2a) under the effective confining pressures investigated here.

[21] Samples deformed to different axial strains confirm the multiple presence of deformation bands (Figure 4), with the sample deformed to 4% strain only showing a few deformation bands while the sample deformed to 10% strain has several bands, with visible host rock lenses between

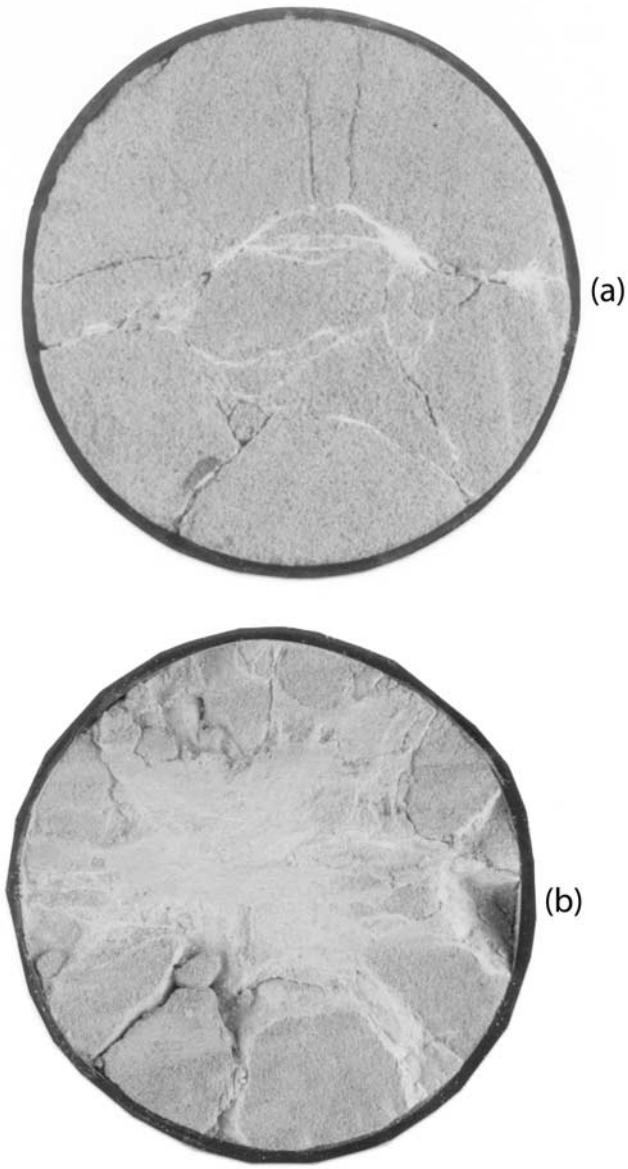

Figure 4. Radial, whole sample photographs of surfaces perpendicular to the axial direction of the core, showing the geometry of the fault zone at two different total axial strains: (a) 4% strain and (b) 10% strain. Note the increasing width of the fault zone, which parallels an increase in the number of discrete strands. Samples are 100 mm in diameter. Note again some open fractures.

them. Meanwhile, the effect of increasing effective confining pressure appears to be to increase the width of the fault zone in general (Figure 5), suggesting transition to more pervasive damage, as also observed by *Mair et al.* [2002]. For example, the sample deformed at 34.5 MPa effective confining pressure has a wider fault zone relative to the sample at 20.7 MPa despite an identical total axial strain. This observation for the deformation of large samples contrasts with those of *Crawford* [1998], who reported an inverse relationship between shear zone thickness and normal stress for 38 mm diameter samples that failed in a single strand. However, it is consistent with observations by *Tuefel* [1987], who found an increase in fault zone width with increasing confining pressure using 48mm diameter samples. These discrepancies lend weight to the possibility that the structural evolution of the fault zone in laboratory tests may depend to first order on sample size to grain-size ratio.

3.2. Permeability and Volume Changes

[22] Figure 6 shows typical trends for differential stress (Figure 6a), permeability (Figure 6b), and volumetric strain (Figure 6c) as a function of axial strain during deformation at different effective confining pressures. Also included is the volumetric strain sensitivity parameter (λ_I) for the

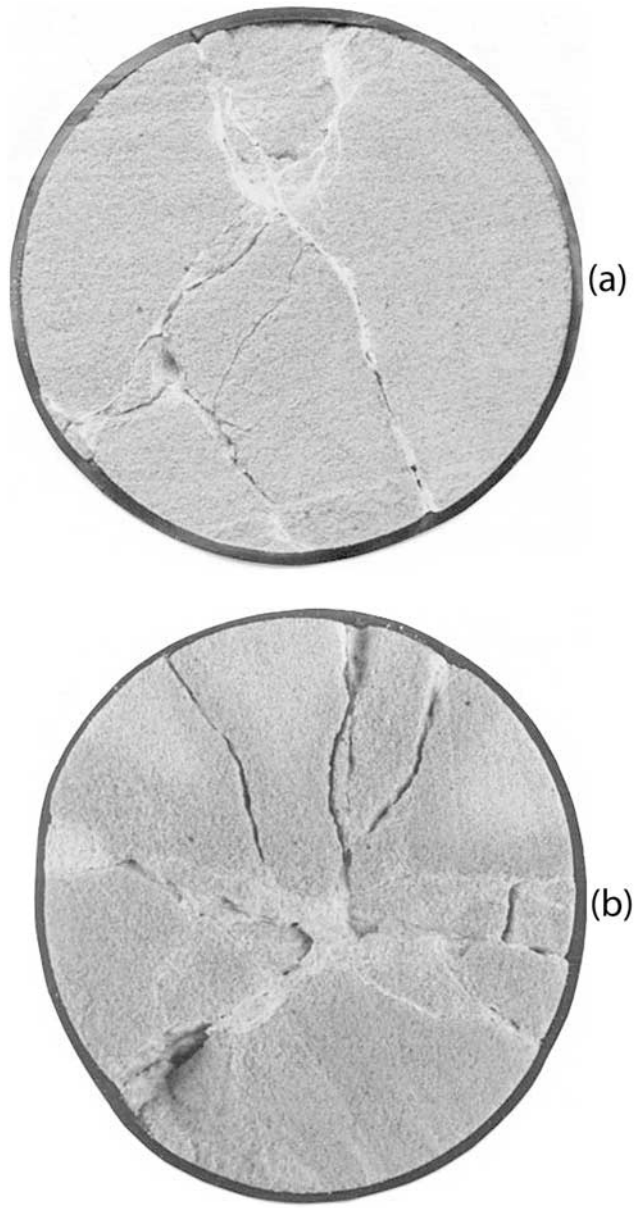

Figure 5. Radial surface of samples cut perpendicular to the axial flow direction, showing an increase in the damage volume of the sample with increasing effective confining pressure: (a) 20.7 MPa and (b) 34.5 MPa. Note again some open fractures.

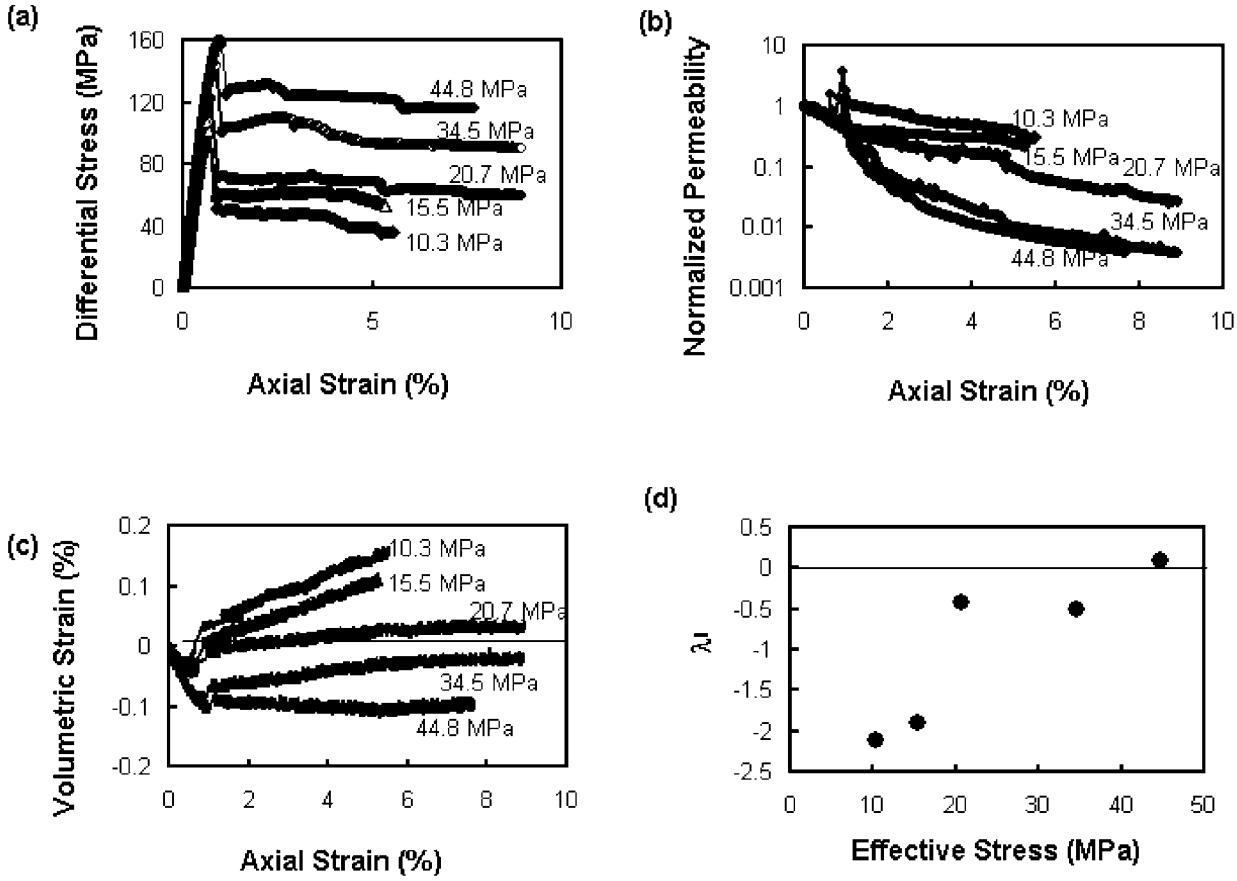

Figure 6. Comparison of the strain-dependent changes in (a) differential stress, (b) permeability, and (c) volumetric strain at different effective confining pressures. Note the increase in permeability after failure for the sample at low effective pressure (10.3 MPa) relative to the initial hydrostatic permeability (Figure 6b), which is due to the large dilatant deformation (Figure 6c). An increase in effective confining pressure is associated with high rates of permeability impairment at relatively low axial strains. Figure 6d is a plot of the slope of volumetric strain against axial strain in the postfailure phase (λ_I), showing inversion in sign from negative slopes up to 34.5 to a positive slope at 44.8 MPa, suggesting compactive deformation at 44.8 MPa.

postfailure phase plotted against effective confining pressure (Figure 6d). This parameter is the slope of the lines shown in Figure 6c for the postfailure regime. Permeability, which has been normalized to the value at the initial (hydrostatic) stress for each sample, shows an exponential dependence on axial strain in the prefailure phase, where the sample undergoes linear-elastic compaction, as shown by the volumetric strain (Figure 6c). Permeability then increases slightly after the yield stress is attained and the sample undergoes dilatant strain hardening. These trends are consistent with observations reported for other high-porosity siliclastic rocks at low confining pressure [e.g., *Zhu and Wong*, 1996, 1997]. The transition from dilatant microcracking to dynamic stress drop is associated with a dramatic increase in apparent permeability. This change occurs over a timescale that is shorter than the time taken to establish steady state differential pressure after a step change in flow rate. The permeability transient is therefore not a true permeability increase, but is likely to be due to the rapid rate of dilatancy associated with nucleation and slip of the fault, which results in a sudden increase in storage capacity of the sample. The measured differential pressure is thus associated with nonsteady flow and is likely to be consistent with the "suction pump" model of *Rudnicki and Chen* [1988], modified for the boundary conditions of constant flow rate [*Main et al.*, 2001; *Grueschow et al.*, 2003].

[23] Permeability and volumetric strain are negatively correlated in the postfailure phase, with the bulk permeability decreasing with increasing strain toward an asymptotic value that depends on the effective pressure. The permeability decreases despite macroscopic sample dilation, as shown by volumetric strain in Figure 6c. This behavior is due to the dominance of cataclastic permeability impairment on the fault over bulk sample dilatancy. In some cases, we observe small spikes in permeability whenever macroscopic stress drops occur during quasi-static postfailure sliding, as exemplified by jumps in permeability at about 5% and 7.5% strain in the 20.7 MPa data (compare Figure 6a with Figure 6b).

[24] Effective confining pressure has a significant effect on the strain-dependent evolution of permeability, as also observed by *Zoback and Byerlee* [1976] on unconsolidated Ottawa Sand. Samples deformed at a low effective stress (10.3 MPa) show an increase in permeability relative to initial values early in the postfailure phase, presumably due to the large dilatant deformation (Figure 6c). However, the permeability becomes highly nonlinear and approaches an asymptotic value at much lower strains as the effective confining pressure increases, shifting the curves to lower strains, consistent with other studies [e.g., *Zoback and Byerlee*, 1976; *Tuefel*, 1987; *Zhu and Wong*, 1997]. This implies that the fault becomes a more effective flow barrier at high effective confining pressures, presumably due to the higher cataclastic intensity [*Crawford*, 1998] evident from grain-size analysis (Figure 2d) and a wider damage zone. This behavior may also reflect the predominance of shear-enhanced compaction at high effective confining pressures [*Wong et al.*, 1997], since samples at high effective confining pressures remain in the compaction regime throughout the quasi-static sliding phase of deformation (Figure 6c).

[25] The inference that compaction dominates behavior at higher effective confining pressures can be quantified by noting that in Figure 6c, the volumetric strain has a nearly linear relationship with axial strain in the postfailure stage and can be approximated by

$$d\Delta = -\lambda_I(\varepsilon - \varepsilon_c), \tag{4}$$

where λ_I is the proportionality constant (strain sensitivity parameter). We find that an increase in volume (dilatancy) relative to the volume at critical strain implies $\lambda_I < 0$ (axial strain is defined positive for shortening), while $\lambda_I > 0$ for compaction. Figure 6d shows a plot of λ_I against effective confining pressure, and we note that λ_I is negative for all but the sample at 44.8 MPa. Moreover, λ_I values become more positive with increasing effective confining pressure, implying a systematic decrease in volume dilatancy at a given strain as effective stress increases. What is not clear is whether these volume changes occur in the matrix or in the fault zone, a question that is beyond the scope of this study.

4. Analysis and Interpretation

[26] We have documented results from experiments in which fluid permeability was monitored primarily as a function of axial strain while deforming each core at a constant axial displacement rate, flow rate and effective confining pressure. Experiments conducted at different effective confining pressures were then used to investigate the role of effective confining pressure on the observed permeability evolution. Central to this design philosophy was an attempt to link permeability changes to the evolving pore structure, which is strongly dependent on effective mean stress [*Wong et al.*, 1997] and also on primary petrophysical properties of the samples [*Zhu and Wong*, 1996; *Popp et al.*, 2001]. First, we have observed a nonlinear decay in permeability with increasing axial strain after failure, this occurring in spite of the bulk sample experiencing overall dilation. Second, despite differences in sample attributes and chemical environment, we have confirmed that the fault zone evolves by increasing the number of deformation bands while the grain-size distribution in each band remains constant, regardless of total axial strain [*Mair et al.*, 2000]. This demonstrates that the results may be generally applicable to porous siliclastic rocks. Third, the rate of postfailure permeability impairment increases dramatically at higher effective confining pressures, consistent with a more effective comminution process [*Tuefel*, 1987; *Crawford*, 1998] and/or predominance of shear-enhanced compaction [*Wong et al.*, 1997]. The shear-enhanced permeability reduction can be anywhere between 1 and 3 orders of magnitude relative to the hydrostatic value measured at the start of the test, depending on the effective pressure. In this section, we use these observations to place quantitative constraints on the evolution of fault zone permeability, by analyzing the data using a constitutive model for fault zone permeability as a function of inelastic axial strain and effective confining pressure during active deformation. We begin by discussing the apparent paradox of decreasing permeability with inelastic axial strain on the fault, which occurs against an increase in volumetric strain, as shown in Figure 6.

4.1. Evolution of the Flow Path

[27] Changes in permeability during loading of rocks can generally be related directly to changes in porosity due to mechanical processes occurring at the grain scale [*Popp et al.*, 2001]. These processes include microcrack induced dilatancy and cataclastic compaction. During triaxial loading, initial elastic deformation can lead to either strain localization due to dilatant microfracturing or shear-enhanced compaction due to pore collapse and Hertzian fracturing [*Menendez et al.*, 1996]. Either way, these grain-scale processes lead to changes in bulk sample porosity (ϕ) and hence permeability (k). The latter depends on interconnected porosity, and the relationship between the two is often rationalized via the empirical Kozeny-Carman equation [*Bruno*, 1994]:

$$k = \frac{\phi^3}{C\tau^2 S^2}, \tag{5}$$

where C is a pore geometry factor, τ is the tortuosity of the flow path, and S is the specific surface area per unit volume of the porous medium. However, experimental measurements often show that over a narrow range of porosity, it is impossible to distinguish between the power law form given in equation (5) and the exponential form, which is often used for high-porosity sandstones [e.g., *Zhu and Wong*, 1997]. We adopt the exponential form here in order to maintain consistency with these previous studies:

$$k = k_c \exp(\eta\phi), \tag{6}$$

where η is the rate dependence of the natural logarithm of permeability on porosity and contains the geometric parameters, including tortuosity.

[28] Our results suggest that permeability evolution during deformation is controlled by the evolving geometry of the flow path, via a complex interplay between matrix compaction/dilatancy and the increasing heterogeneity due to progressive formation of deformation bands. Figure 7 shows graphs of the measured bulk permeability against bulk

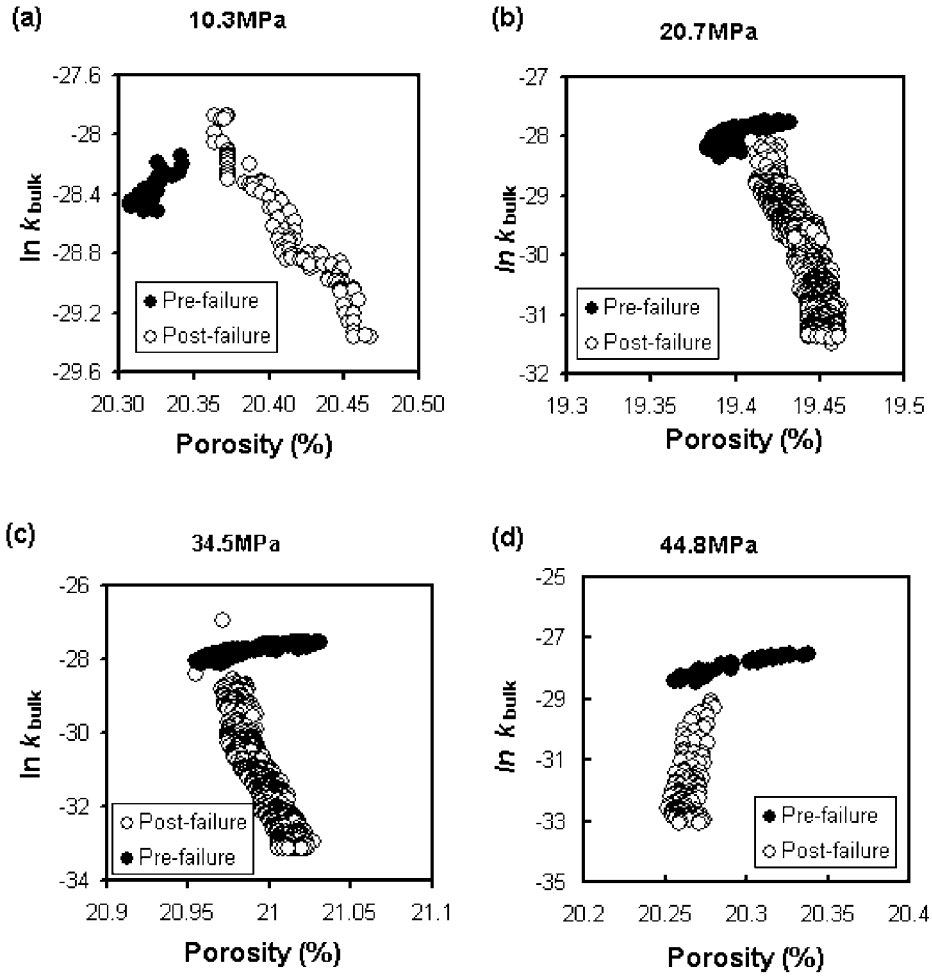

Figure 7. Permeability evolution during triaxial deformation of samples at different effective confining pressures for selected samples, plotted in permeability-porosity space. Note the large decrease in porosity rebound and the change in slope from negative to positive for the postfailure data at high confining pressures (Figure 7d). These slopes appear to correlate with a change in mode of deformation from dilatant brittle deformation toward distributed, shear-enhanced compaction.

porosity, based on equation (6) at four effective confining pressures. They represent the full deformation cycle from initial axial loading (solid symbols) to quasi-stable sliding (open symbols). Firstly, the degree of dilatancy at failure decreases systematically with increasing effective confining pressure. At low effective confining pressures, the predominance of dilatant deformation is manifest in an increase in permeability beyond initial hydrostatic permeability and the value at peak stress (Figure 7a). This phenomenon, which results in increased system storativity may also be responsible for increased hydrologic flows in river basins following earthquakes [*Rojstaczer et al.*, 1995]. Higher effective confining pressures suppress this "suction pump" phenomenon, so that at 44.8 MPa, the value of permeability immediately after failure is lower than that at peak stress despite a modest recovery in porosity. Meanwhile intermediate effective confining pressures lead to some degree of recovery in both porosity and permeability.

[29] A second feature of our results is that bulk sample porosity and permeability are negatively correlated at all effective confining pressures in the postfailure data (except at 44.8 MPa), in direct contradiction to equation (6). The bulk η values are positive for prefailure data and are effectively independent of effective confining pressure (Figure 8a), while postfailure values for the bulk sample become more negative with increasing effective stress up to 34.5 MPa, followed by a sudden reversal to a positive value at 44.8 MPa. Thus globally, equation (6) does not hold for most of the postfailure regime, although this need not imply that locally, η could be not be positive. As already demonstrated above and in numerous previous studies [e.g., *Zhu and Wong*, 1997], positive η values are generally indicative of compactive deformation in high-porosity materials. In effect therefore, the inversion in sign in the postfailure η from 34.5 to 44.8 MPa implies a change in mode of deformation from dilatant to compactive deformation overall. This change in mode of deformation is confirmed by plotting the mechanical data for our tests in the ϕ-q space of *Wong et al.* [1997], which shows transition from shear-induced dilatancy to shear enhanced compaction, relative to

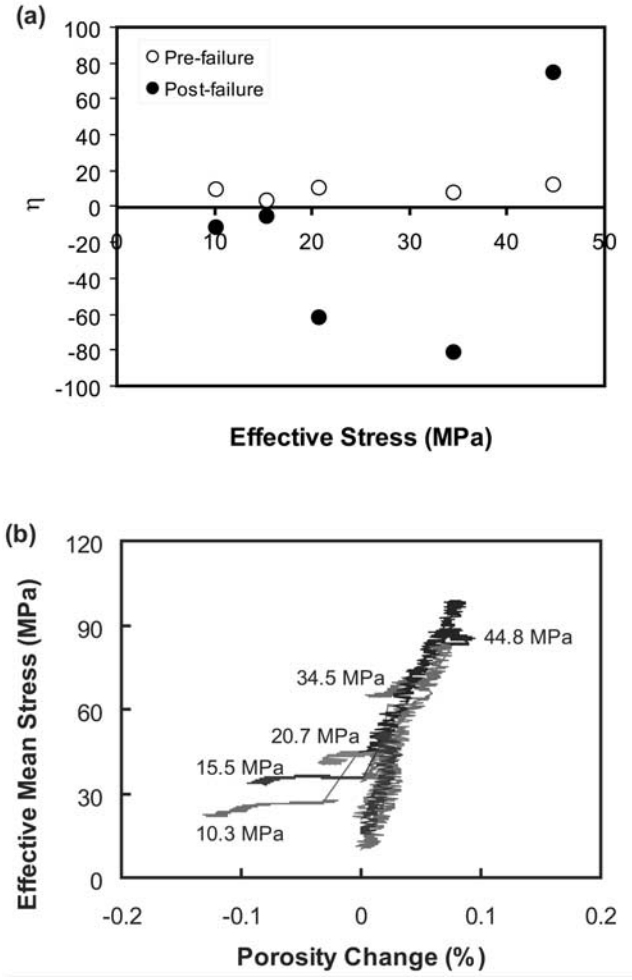

Figure 8. (a) Variation in slopes (η) in the Kozeny-Carman plots from Figure 7, with effective confining pressure for prefailure and postfailure data. (b) Effective mean stress versus porosity change at different effective confining pressures. Note dilatant behavior for samples up to 34.5 MPa, while the sample at 44.8 MPa shows transition to cataclastic flow, which corresponds to the inversion in sign of η for postfailure data (see text for details).

hydrostatic loading, at 44.8 MPa effective confining pressure (Figure 8b). All our tests follow the same path during poroelastic compaction, corresponding to the hydrostatic envelope shown by *Wong et al.* [1997]. For tests up to 34.5 MPa effective confining pressure, samples start to dilate prior to failure, as indicated by a negative porosity change relative to the hydrostatic envelope. Meanwhile, the sample deformed at 44.8 MPa effective confining pressure is transitional and shows a tendency toward shear-enhanced compaction, as indicated by a small positive porosity change. This transition pressure is close to that measured for the Adamswiller Sandstone by *Wong et al.* [1997], although the comparison is only qualitative given the different material properties of the two sandstones and the differences in experimental configuration.

[30] The systematic changes in the bulk value of η therefore provide a macroscopic view of the evolution of the pore-scale flow path during strain-dependent deformation in high-porosity rocks, from dilatant deformation to shear-enhanced compaction. Specifically, we infer that at low effective pressure, the decrease in permeability due to progressive formation of deformation bands is balanced by dilatancy in the matrix, which reduces the overall rate at which permeability declines with increasing strain. Meanwhile, matrix dilatancy is suppressed at higher effective confining pressure due to shear-enhanced compaction, resulting in cooperative effects between the matrix and deformation bands in reducing bulk permeability. In summary, equation (6) assumes that locally, $\eta > 0$ while globally, it is not, and may be negative due to dominance of the fault or matrix anisotropy. In the following section, we attempt to quantify the relative contribution of these two geometrical constraints on the measured permeability as a function of strain.

4.2. Permeability Evolution During Development of Deformation Bands

[31] We will adopt the model of *Main et al.* [2000], captured in equation (3) to evaluate the relative contribution of matrix deformation and cataclastic comminution to permeability evolution during progressive formation of deformation bands. The aim is to relate observed permeability trends in the postfailure regime to the evolving flow path discussed above, and to show how this evolution depends on effective confining pressure.

[32] Figure 9 shows plots of the data and fits to equation (3) at four selected effective confining pressures, corresponding to the tests used in Figure 7. The curves were fitted using an iterative nonlinear regression technique [*Ngwenya et al.*, 2001], and confirm that the three-parameter model fits the data with high correlation coefficients, ranging from 0.970 to 0.987. It is also apparent in Figure 9 that the relationship is log linear at low effective confining pressures, but becomes increasingly nonlinear as effective confining pressure increases. The fitting parameters to the data for all tests discussed in this paper are collected in Table 1. Values of the first-order term (a_1) are negative for all tests, while the second-order term (a_2) is positive for most of the tests. Thus the first-order feature is an exponential sealing with respect to strain, corrected for sample shortening ($\delta/1-\delta$), whereas the second-order term introduces a positive curvature in the data that is more important at high effective confining pressures. The a_2 term depends only on the permeability change in the matrix and reflects the transition from more dilatant to more compactant deformation. Both parameters vary systematically with effective stress; a_1 values decrease, while a_2 values increase systematically with effective confining pressure (Figure 10a). The linear regression coefficients in Figure 10a can be combined with equation (3a) to yield a macroscopic constitutive law for bulk sample permeability in stress-strain space; thus

$$\ln k_{bulk} = \ln k_c + \left\{(16.0 - 2.89P_e)\left(\frac{\delta}{1-\delta}\right)\right\} + \left\{(28.5P_e - 368)\left(\frac{\delta^2}{1-\delta}\right)\right\} \quad (7)$$

with permeability in m^2 and effective stress (P_e) in MPa. Values of bulk permeability (k_{bulk}) predicted by equation (7)

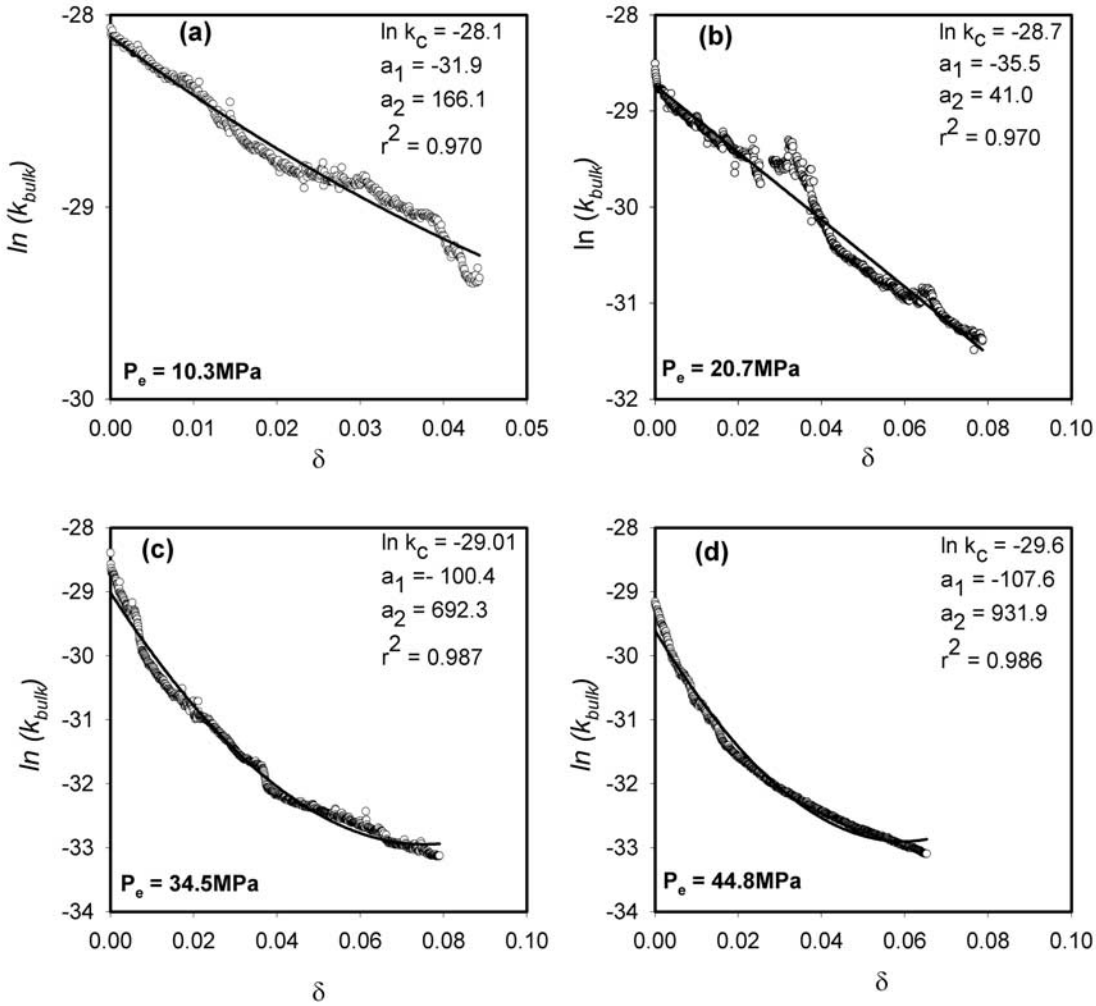

Figure 9. Comparison of experimental data in the postfailure regime (unfilled circles) with model predictions (solid lines) based on equation (3) for tests at four effective pressures. Note the increasing curvature in the data in the model predictions at high effective pressures, which parallels the increasing compaction term, a_2. The model curve starts to deviate from the experimental data at high strains for high effective confining pressures.

for the Clashach sandstone are shown in Figure 10b. We note that the contours are fairly tight at high effective confining pressures, consistent with the rapid permeability impairment during slip shown in Figure 6b. In addition, the contours diverge slightly above 35 MPa effective confining pressure, implying some recovery in permeability with increasing slip. This paradoxical outcome may arise because faults have a tendency to dilate slightly at high shear strains [*Zhang and Tullis*, 1998]. Because shear-induced dilation can also increase microstructural and hydraulic anisotropy, a relative increase in permeability with strain will only occur at high effective stresses, where the fault zone is pervasive (Figure 5). In general, the constitutive equation appears to slightly overestimate the permeability at high effective confining pressures (see also curve fits in Figure 9). Nevertheless, within the parameter range investigated here, equation (7) adequately predicts the evolution of bulk permeability as a function of effective confining pressure and postfailure strain. We believe that the model parameters will vary depending on the mechanical properties of the

Table 1. Test Conditions and Hydraulic and Constitutive Model Parameters for Experiments in This Study

Sample	P_e, MPa	L, m	k_o, m^2	ε_c, %	l_c, m	k_c, m^2	a_1	a_2
CLS13	10.3	0.217	$10^{-12.2}$	0.86	0.215	$10^{-12.2}$	−31.9 ± 0.7	166.1 ± 16
CLS16	15.5	0.2000	$10^{-12.3}$	0.86	0.198	$10^{-12.7}$	−8.49 ± 0.4	−87.2 ± 9.1
CLS15	20.7	0.218	$10^{-12.0}$	0.93	0.216	$10^{-12.5}$	−35.5 ± 0.8	41 ± 10
CLS12	34.5	0.216	$10^{-12.0}$	0.87	0.215	$10^{-12.6}$	−100.4 ± 0.7	692.3 ± 8.7
CLS14	44.8	0.217	$10^{-11.9}$	1.16	0.215	$10^{-12.8}$	−107.6 ± 0.8	931.9 ± 124

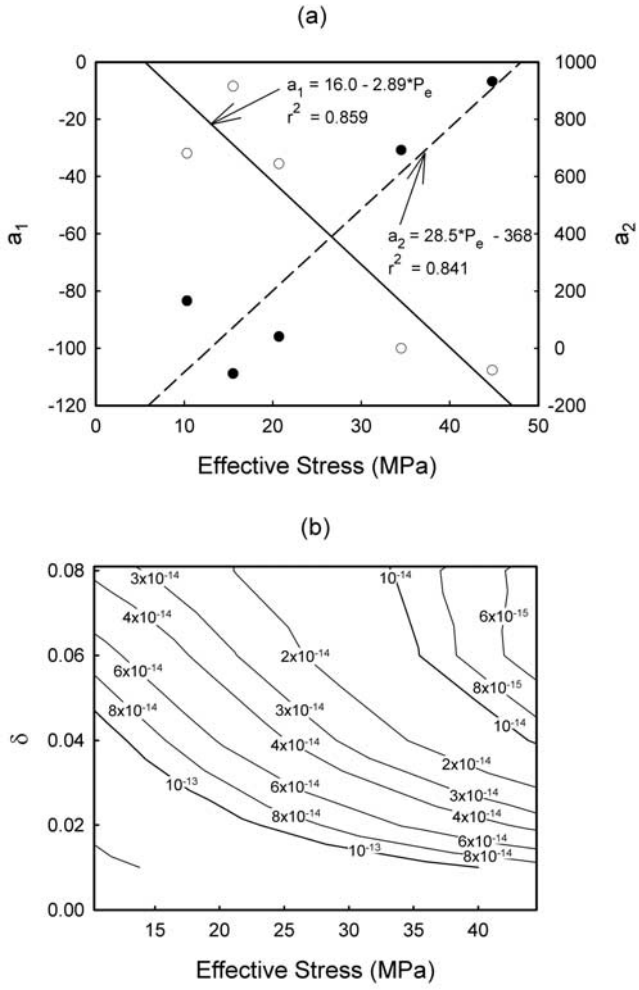

Figure 10. (a) Graphical summary of the variation of a_1 (open circles) and a_2 (solid circles) with effective confining pressure. Both parameters vary linearly with effective confining pressure, with a_1 decreasing while a_2 increases. In Figure 10b, bulk permeability (m^2) predicted by the new constitutive model according to equation (7) is plotted in strain-effective pressure space. The symbol (δ) is defined in the text as the axial strain after failure.

intact sandstone, and thus will need to be determined for each rock type. Our future experiments will address this important question.

5. Discussion

[33] Given that only bulk permeability measurements are possible in this type of triaxial deformation experiment, another motivation for developing this model was to allow some estimate of the permeability of single strands from the bulk measurements. *Crawford* [1998] suggested such a methodology for single shear bands using 38mm diameter samples, which assumes that after fracture the measured pressure drop across the sample is almost entirely due to shear band sealing. While his model was successful in predicting sealing rates, the underlying assumption is limited in its application, being valid only for cases where the matrix permeability is much higher than potential shear band permeability [*Crawford*, 1998]. Furthermore, this approach cannot account for matrix compaction and/or dilatancy and may therefore both overestimate and underestimate fault seal intensities.

[34] On the other hand, it is possible to estimate shear zone permeability from the model parameters a_1 and a_2 for any matrix/fault permeability contrast, since the deformation band permeability (k_{strand}) is explicitly accounted for in equation (3b). Unfortunately, we currently do not have a method for independently evaluating γ_I from the experimental data. A reasonable estimate of γ_I may be made from a_2 (equation (3c)); thus

$$\gamma_I = \frac{a_2}{\left(1 + \frac{w_o}{l_c}\right)}, \tag{8}$$

provided that w_o is independently known at each effective confining pressure. To illustrate the dependence, we measured fault zone thickness at atmospheric pressure for several cores deformed to different axial strains at a constant effective confining pressure of 20.7 MPa, after cutting them perpendicular to the axial strain. These measurements are plotted against axial strain in Figure 11, from which we recover w_o = 0.044 m, a value that is valid for an effective confining pressure of 20.7 MPa. Inserting this value into equation (8) for CLS15 (Table 1), which was also conducted at P_e = 20.7 MPa yields γ_I = 34.1. The permeability of individual strands for this fault zone can then be estimated by rearranging equation (3b) to give

$$\ln k_{strand} = \ln k_c + \frac{l_c}{w_o}(a_1 + \gamma_I). \tag{9}$$

Using values in Table 1 for this test and the estimated value of γ_I yields $k_{strand} \approx 3.46 \times 10^{-16}$ m^2, so that with the

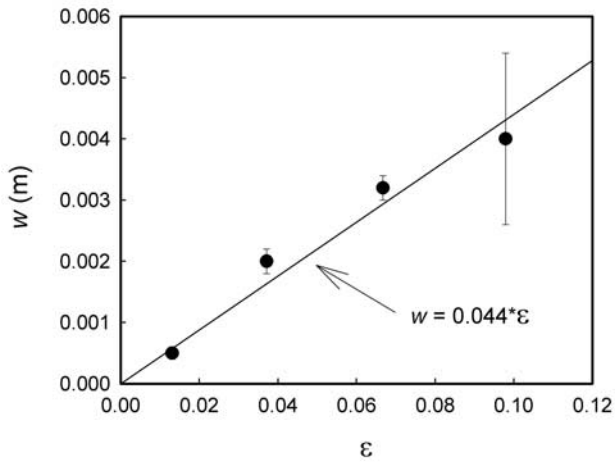

Figure 11. Graph showing the variation in width of fault zone with total axial strain for tests at 20.7 MPa. Each data point is an average of two measurements, with the errors being one times the standard deviation on the mean. In theory, the graph should have a positive intercept on the strain axis, since deformation bands do not start forming until strain is ~0.09. As the actual measurements do not conform to this, the regression line has been forced through the origin and yields a slope (w_o) of 0.044 m (see text for use of this slope).

hydrostatic permeability (k_o) of 10^{-12} m^2, $k_o/k_{strand} = 2.9 \times 10^3$. This predicts strand permeability that is 3.5 orders of magnitude lower than the intact sample under hydrostatic confinement. This contrast is remarkably close to values estimated for single shear bands by *Crawford* [1998] but slightly higher than those reported by *Gibson* [1998] for intact sandstone cores containing cataclastic and solution deformation bands.

[35] As pointed out above, the calculated permeability contrast is only an order of magnitude estimate. This is because our permeability model does not take into account the angle of the zone of deformation bands in defining the flow path [see *Main et al.*, 2000]. As shown by *Taylor et al.* [1999], fluid flowing across inclined fractures in permeable rock matrices will be refracted at the fracture-matrix interface, requiring the angle of refraction and hence of the fracture to be taken into account. However, although we can measure the general orientation of the fault (Figure 3), its internal geometry is complex, consisting of anastomosing deformation bands with different segments of the same band having different orientations (from axial through inclined to normal). Given that our simplified model gives reasonably good statistical description of the data, with correlation coefficients greater than 0.97, and given the complexity of the flow path, it is questionable whether a more complicated model with inherently more parameters is justified. This is especially the case since *Ogilvie et al.* [2001] have shown that bulk permeability measurements grossly overestimate k_o/k_{strand} ratios even for cases where the right orientation is used [e.g., *Sverdrup and Bjorlykke*, 1992]. It follows that the estimates of k_{strand} and therefore the permeability contrasts are probably a lower bound and must be treated as order of magnitude estimates only.

[36] The requirement for a priori determination of w_o precludes an evaluation of the systematic changes in k_{strand} with effective confining pressure. *Crawford* [1998] noted a linear decrease in shear band width with increasing normal stress for small samples, implying a decrease in w_o, and found that higher normal stresses resulted in higher matrix/band permeability contrasts. Thus fault strand permeability dropped mainly by a decrease in grain size and sorting, in contrast to the relatively constant fault gouge size distribution given here and by *Mair et al.* [2002]. According to our data (Figure 5) and that of *Mair et al.* [2002], w_o should increase with increasing effective confining pressure owing to deformation by distributed shear-enhanced compaction at high pressures. Parallel tests using small samples in the current study suggest that both trends are valid, again reflecting the first-order dependence of microstructural evolution on sample/grain-size ratio. For now, we predict that for the case of w_o increasing with effective confining pressure, the permeability contrast will increase with increasing effective pressure to a maximum, after which the contrast will approach unity as deformation becomes distributed and the whole sample compacts. We are currently testing this hypothesis on a new suite of tests at different ultimate strains.

[37] Examination of equation (3c) shows that a positive a_2 implies positive γ_I since by definition w_0 and l_c are positive, as was demonstrated with the calculation above. With strain-scale matrix permeability evolving according to equation (2), this implies further that in most of our tests, the axial matrix permeability is decreasing, despite sample dilation (Figures 6c and 6d). This apparent paradox has been attributed to the anisotropic permeability tensor because of the development of cracks parallel to the axial direction to produce overall sample dilatancy, coupled with closing of pores perpendicular to this direction [*Zhu and Wong*, 1996]. The overall result is an increase in tortuosity of the flow path which can account for matrix permeability impairment in the axial direction, despite overall sample dilatancy [*Zhu and Wong*, 1996; *Main et al.*, 2000].

6. Conclusions

[38] In summary, we have presented results from a suite of experiments in which permeability evolution was monitored as a function of axial strain at different constant effective confining pressures. The permeability of all our samples followed a three-stage strain-dependent evolution. The first stage is a linear decrease prior to sample failure, which is associated with poroelastic compaction of the matrix. The second stage shows a transient increase in permeability and is associated with dynamic stress drop, which is interpreted to be a suction pump effect due to rapid dilatant slip. This phase was followed by the third stage (postfailure) characterized by a systematic quasi-static decrease in permeability during inelastic axial strain on the fault. This decrease occurs despite the fact that the bulk sample undergoes dilatant deformation.

[39] The first and third stages of deformation may be linked directly to the microstructural evolution of the flow path, which occurs via a complex interplay between matrix compaction/dilatancy and cataclastic fault sealing. In the prefailure stage, permeability and porosity are positively correlated via a proportionality constant (η) that is essentially independent of effective pressure, and is dominated by hydrostatic compaction [*Zhu and Wong*, 1997]. Postfailure (third stage) bulk permeability is negatively correlated to bulk porosity at low effective pressure, but η becomes positive at high effective pressures, implying transition from dilatant to compactive behavior.

[40] Microstructural studies confirm that postfailure strain is accommodated by progressive formation of new bands, leading to complex fault zone geometry, where fault zone width and the number of bands increase linearly with inelastic axial strain. The data has been analyzed using a new model [*Main et al.*, 2000] for permeability evolution during the sequential formation of deformation bands. The model takes into accounts the observed fault zone geometry, allowing a first-order estimate of the permeability of individual deformation bands from bulk sample values, provided that the rate of growth of the fault zone is known. The model parameters vary systematically with confining pressure, and may thus provide a methodology for predicting fault permeability and sealing potential as a function of burial depth and total inelastic axial strain. As such, equation (3) represents the first quantitative algorithm for predicting fault permeability in subsurface settings involving sand-sand contacts in cases where clay smears are absent.

[41] **Acknowledgments.** The experimental work presented here was supported through an oil industry consortium consisting of BP-Amoco,

ExxonMobil, Lasmo, Shell, Statoil, and the Japanese National Oil Corporation (JNOC). The work benefited from constructive discussions with Jan Konstanty, Jonathan Craig, Andrew McCann, Miki Takahashi, David Yale, Kes Heffer, Chris Townsend, Bill Shea, Brian Crawford, and Fredrick Dula. Ben Finney, Mike Hall, and Alex Jackson provided valuable laboratory support, while Yvonne Fletcher helped with photography. We would also like to thank Attila Aydin, Dan Faulkner, and David Mainprice for constructive reviews that improved the clarity of our contribution.

References

Antonellini, M. A., and A. Aydin, Effect of faulting on fluid flow in porous sandstones: Petrophysical properties, *AAPG Bull.*, *78*, 355–377, 1994.

Antonellini, M. A., A. Aydin, and D. D. Pollard, Microstructure of deformation bands in Porous sandstone at Arches National Park, Utah, *J. Struct. Geol.*, *16*, 941–959, 1994.

Aydin, A., Small faults formed as deformation bands in sandstone, *Pure Appl. Geophys.*, *116*, 913–930, 1978.

Aydin, A., and A. M. Johnson, Development of faults as zones of deformation bands and slip surfaces in sandstone, *Pure Appl. Geophys.*, *116*, 931–942, 1978.

Beach, A., A. I. Welbon, P. J. Brockbank, and J. E. McCallum, Reservoir damage around faults: Outcrop examples from the Suez rift, *Pet. Geosci.*, *5*, 109–116, 1999.

Bruno, M. S., Micromechanics of stress-induced permeability anisotropy in sedimentary rock, *Mech. Mater.*, *18*, 31–48, 1994.

Caine, J. S., J. P. Evans, and C. B. Forster, Fault zone architecture and permeability structure, *Geology*, *24*, 1025–1028, 1996.

Crawford, B. R., Experimental fault sealing: Shear band permeability dependency on cataclastic fault gouge characteristics, in *Structural Geology in Reservoir Characterization*, edited by M. P. Coward, S. Daltaban, and H. Johnson, *Geol. Soc. Spec. Publ.*, *127*, 27–47, 1998.

Evans, J. P., C. B. Forster, and J. V. Goddard, Permeability of fault-related rocks, and implications for hydraulic structure of fault zones, *J. Struct. Geol.*, *11*, 1393–1404, 1997.

Fowles, J., and S. D. Burley, Textural and permeability characteristics of faulted, high porosity sandstones, *Mar. Pet. Geol.*, *11*, 608–623, 1994.

Gibson, R. G., Physical character and fluid flow properties of sandstone-derived fault zones, in *Structural Geology in Reservoir Characterization*, edited by M. P. Coward, S. Daltaban, and H. Johnson, *Geol. Soc. Spec. Publ.*, *127*, 83–97, 1998.

Grueschow, E., O. Kwon, I. G. Main, and J. W. Rudnicki, Observations and modeling of the suction pump effect during rapid dilatant slip, *Geophys. Res. Lett.*, *30*(5), 1226, doi:10.1029/2002GL015905, 2003.

Hippler, S. J., Deformation microstructures and diagenesis in sandstone adjacent to an extensional fault: Implications for the flow and entrapment of hydrocarbons, *AAPG Bull.*, *77*, 625–637, 1993.

Jamison, W. R., and D. W. Stearns, Tectonic deformation of the Wingate sandstone, Colorado National Monument, *AAPG Bull.*, *76*, 2584–2608, 1992.

Knipe, R. J., Faulting processes and fault seal, in *Structural and Tectonic Modelling and Its Application to Petroleum Geology*, edited by R. M. Larsen et al., *Spec. Publ. 1*, pp. 325–342, Norw. Pet. Soc., Trondheim, 1992.

Knipe, R. J., G. Jones, and Q. J. Fisher, Faulting, fault sealing and fluid flow in hydrocarbon reservoirs: An introduction, in *Faulting, Fault Sealing and Fluid Flow in Hydrocarbon Reservoirs*, edited by G. Jones, Q. J. Fisher, and R. J. Knipe, *Geol. Soc. Spec. Publ.*, *147*, vii–xxi, 1998.

Knott, S., A. Beach, P. J. Brockbank, J. L. Brown, J. E. McCallum, and A. I. Welbon, Spatial and mechanical controls on normal fault populations, *J. Struct. Geol.*, *18*, 359–372, 1996.

Main, I. G., B. G. D. Smart, G. B. Shimmield, S. C. Elphick, B. Crawford, and B. Ngwenya, The effects of combined changes in pore-fluid chemistry and stress state on permeability in reservoir analogues, in *North Sea Oil and Gas Reservoirs III*: *Proceedings of the 3rd North Sea Oil and Gas Reservoirs Conference*, edited by J. O. Aasen et al., pp. 357–370, Kluwer Acad., Norwell, Mass., 1994.

Main, I. G., O. Kwon, B. T. Ngwenya, and S. C. Elphick, Fault sealing during deformation-band growth in porous sandstone, *Geology*, *28*, 1131–1134, 2000.

Main, I., K. Mair, O. Kwon, S. Elphick, and B. Ngwenya, Experimental constraints on the mechanical and hydraulic properties of deformation bands in porous sandstones: A review, in *The Nature and Significance of Fault Zone Weakening*, edited by R. E. Holdsworth et al., *Geol. Soc. Spec. Publ.*, *186*, 43–63, 2001.

Mair, K., I. G. Main, and S. C. Elphick, Sequential development of deformation bands in the laboratory, *J. Struct. Geol.*, *22*, 25–42, 2000.

Mair, K., S. Elphick, and I. Main, Influence of confining pressure on the mechanical and structural evolution of laboratory deformation bands, *Geophys. Res. Lett.*, *29*(10), 1410, doi:10.1029/2001GL013964, 2002.

Manzocchi, T., J. J. Walsh, P. Nell, and G. Yielding, Fault transmissibility multipliers for flow simulation models, *Pet. Geosci.*, *5*, 53–63, 1999.

Menendez, B., W. Zhu, and T.-f. Wong, Micromechanics of brittle faulting and cataclastic flow in Berea sandstone, *J. Struct. Geol.*, *18*, 1–16, 1996.

Moore, D. E., and D. A. Lockner, The role of micro-cracking in shear-fracture propagation in granite, *J. Struct. Geol.*, *17*, 95–114, 1995.

Ngwenya, B. T., S. C. Elphick, and G. B. Shimmield, Reservoir sensitivity to water flooding: An experimental study of seawater injection in North Sea reservoir analogs, *AAPG Bull.*, *79*, 285–304, 1995.

Ngwenya, B. T., S. C. Elphick, I. G. Main, and G. B. Shimmield, Experimental constraints on the diagenetic self-sealing capacity of faults in high porosity rocks, *Earth Planet. Sci. Lett.*, *183*, 187–199, 2000.

Ngwenya, B. T., I. G. Main, S. C. Elphick, B. R. Crawford, and B. G. D. Smart, A constitutive Law for low-temperature creep of water-saturated sandstones, *J. Geophys. Res.*, *106*, 21,811–21,826, 2001.

Ogilvie, S. R., J. M. Orribo, and P. W. J. Glover, The influence of deformation bands upon fluid flow using profile permeametery and positron emission tomography, *Geophys. Res. Lett.*, *28*, 61–64, 2001.

Popp, T., H. Kern, and O. Schulze, Evolution of dilatancy and permeability in rock salt during hydrostatic compaction and triaxial deformation, *J. Geophys. Res.*, *106*, 4061–4078, 2001.

Ramsay, J., The crack-seal mechanism of rock deformation, *Nature*, *284*, 135–139, 1980.

Rhett, D. W., and L. W. Teufel, Stress path dependence of matrix permeability on North Sea sandstone reservoir rock, *Proc. U.S. Rock Mech. Symp.*, *33*, 345–354, 1992.

Rojstaczer, S., S. Wolf, and R. Michel, Permeability enhancement in the shallow crust as a cause of earthquake-induced hydrological changes, *Nature*, *373*, 237–239, 1995.

Rudnicki, J. W., and C.-H. Chen, Stabilization of rapid frictional slip on a weakening fault by dilatant hardening, *J. Geophys. Res.*, *93*, 4745–4757, 1988.

Scholz, C. H., Wear and gouge formation in brittle faulting, *Geology*, *15*, 493–495, 1987.

Scott, T. E., and K. C. Nielsen, The effects of porosity on the brittle-ductile transition, *J. Geophys. Res.*, *96*, 405–414, 1991.

Shipton, Z. K., and P. A. Cowie, Damage zone and slip-surface evolution over mm to km scales in high-porosity Navajo Sandstone, Utah, *J. Struct. Geol.*, *23*, 1825–1844, 2001.

Sibson, R., Implications of fault valve behaviour for rupture nucleation and recurrence, *Tectonophysics*, *211*, 283–293, 1992.

Sverdrup, E., and K. Bjorlykke, Small faults in sandstones from Spitsbergen and Haltenbanken: A study of diagenetic and deformation structures and their relation to fluid flow, in *Structural and Tectonic Modelling and Its Application to Petroleum Geology*, edited by R. M. Larsen et al., *Spec. Publ.1*, pp. 507–518, Norw. Pet. Soc., Trondheim, 1992.

Taylor, W. L., D. D. Pollard, and A. Aydin, Fluid flow in discrete joint sets: Field observations and numerical simulations, *J. Geophys. Res.*, *104*, 28,983–29,006, 1999.

Tuefel, L. W., Permeability changes during shearing deformation in fractured rock, *Proc. U.S. Rock Mech. Symp.*, *28*, 473–480, 1987.

Underhill, J. R., and N. H. Woodcock, Faulting mechanisms in high porosity sandstones: New Red Sandstone, in *Deformation of Sediments and Sedimentary Rocks*, edited by M. E. Jones and R. M. F. Preston, *Geol. Soc. Spec. Publ.*, *29*, 91–105, 1987.

Wong, T.-f., C. David, and W. Zhu, The transition from brittle faulting to cataclastic flow in porous sandstones: Mechanical deformation, *J. Geophys. Res.*, *102*, 3009–3025, 1997.

Zang, A., F. C. Wagner, S. Stanchits, C. Janssen, and G. Dresen, Fracture process zone in granite, *J. Geophys. Res.*, *105*, 23,651–23,661, 2000.

Zhang, S., and T. E. Tullis, The effect of fault slip on permeability and permeability anisotropy in quartz gouge, *Tectonophysics*, *295*, 41–52, 1998.

Zhu, W., and T.-f. Wong, Permeability reduction in a dilating rock: Network modelling of damage and tortuosity, *Geophys. Res. Lett.*, *23*, 3099–3102, 1996.

Zhu, W., and T.-f. Wong, The transition from brittle faulting to cataclastic flow: Permeability evolution, *J. Geophys. Res.*, *102*, 3027–3041, 1997.

Zoback, M. D., and J. D. Byerlee, Effect of high-pressure deformation on permeability of Ottawa Sand, *AAPG Bull.*, *60*, 1531–1542, 1976.

S. C. Elphick, I. G. Main, and B. T. Ngwenya, School of GeoSciences, Institute of Geology and Geophysics, University of Edinburgh, West Mains Road, Edinburgh EH9 3JW, UK. (bryne.ngwenya@ed.ac.uk)

O. Kwon, Core Laboratories, 6316 Windfern, Houston, TX 77040, USA.